Battery degradation diagnosis under normal usage without requiring regular calibration data

Ze Wu [1], Yongzhi Zhang [1,*], Huizhi Wang [2,3]

[1] College of Mechanical and Vehicle Engineering, Chongqing University, 400030, Chongqing, China.

[2] Department of Mechanical Engineering, Imperial College London, London SW7 2AZ, United Kingdom.

[3] The Faraday Institution, Harwell Science and Innovation Campus, Didcot OX11 0RA, United Kingdom.

*Corresponding author: Yongzhi Zhang (yzzhangbit@gmail.com, yongzhi@cqu.edu.cn)

Abstract

Lithium-ion batteries undergo capacity loss and power fade over time. Despite indicating degradation, these changes lack internal insights. Degradation modes group various mechanisms but are challenging to quantify due to aging complexity. In this paper, a noninvasive and comprehensive diagnostic framework is proposed for the accurate estimation of the state of health (SOH) and degradation modes. A large amount of synthetic data is generated from the mechanistic model to cover many typical aging paths without using redundant experimental data. A data-driven multistep diagnosis method is developed by using incremental capacity sequences. This method analyses unique sensitivities to voltage responses from different degradation modes and identifies them sequentially to simplify complex interactions. In addition, overpotential correction is incorporated to estimate battery degradation modes under normal usage. This framework is validated through experimental data under various operating conditions, affirming the 2% accuracy of SOH estimation and the effective automatic quantification of degradation modes. Furthermore, the method is applicable to common state-of-charge (SOC) windows ranging from 25%-85% (3.6 V-4.1 V for the voltage window) and a high current rate up to C/4. The diagnostic framework does not rely on any regular calibration data during model training and thus has high potential for practical application.

Keywords: Lithium-ion battery; degradation mode diagnosis; synthetic data generation; machine learning; mechanistic model

1. Introduction

Lithium-ion batteries have garnered considerable attention due to their high capacity and stable charge–discharge cycles [1-4]. They are widely employed in portable electronic devices, electric vehicles and large-scale energy storage systems. The widespread use requires additional functions in battery management systems (BMSs) [5, 6]. A crucial aspect of BMSs is the assessment of battery degradation arising from internal electrochemical reactions and its accumulation over time. Capacity loss and power fade are intuitive indicators of aging, which impacts the durability and performance of devices [7]. To enable the degradation levels to be rationally assessed, the state of health (SOH) has been introduced and defined as the percentage decay of the current capacity relative to the initial capacity or the increase in impedance, serving as a macroscopic criterion for battery performance [8]. However, using SOH as the sole indicator cannot yield a nuanced understanding of battery degradation. Therefore, the internal electrochemical aging process of batteries needs to be reasonably and reliably evaluated.

The degradation process of batteries is highly complex and unpredictable. Under the influence of external operating conditions and environmental temperature, the growth of solid electrolyte interphases (SEI), electrode particle fractures and phase transitions within batteries can accelerate battery failure [9]. Invasive analysis and postfailure disassembly have been at the forefront of attempts to gain a deeper understanding of battery degradation mechanisms [10]. These methods effectively facilitate qualitative analyses of changes in material properties and degradation modes. However, their practical applications are unrealistic and incur high costs. Therefore, noninvasive battery degradation analysis methods have been explored by categorizing battery degradation modes into loss of lithium inventory (LLI) and loss of active material (LAM). Essentially, this approach, which was initially proposed by Dubarry [11, 12], provides a summarized description situated between capacity loss, power fade and internal degradation phenomena.

Noninvasive degradation diagnostic methods include low-current rate voltage vs. capacity (VQ) curve reconstruction, incremental capacity-differential voltage (IC-DV) analysis, electrochemical impedance spectroscopy (EIS) and differential thermal voltage (DTV) methods [10]. Dubarry et al. quantified each degradation mode by constructing VQ curves at low current rates using a mechanistic model combined with IC-DV analysis [13, 14]. The shifting and scaling of the electrode open circuit potential (OCP) curves were linked with modes through a model for quantification. Brikl et al. [15] developed a similar model with parameter variations transferred to the state of charge (SOC) of the OCPs. Note that a reconstructed VQ often uses a full battery or half battery with low-rate charge and discharge. Schmitt et al. [16] considered the actual voltage range and C-rate of the cell to reconstruct the VQ through global optimization. Zhu et al. [17] determined a more suitable range for VQ reconstruction for different degradation modes. However, this model sometimes struggles to ensure accuracy, as the optimized objective is not always applicable to the target VQ. Incremental capacity analysis (ICA) and differential voltage analysis (DVA) have been introduced to enhance precision during VQ reconstruction by indicating phase transitions through differential processing. Yang et al. incorporated DV into the optimization objective during VQ reconstruction to improve accuracy [18]. A crucial issue is that fit-based VQ reconstruction may lead to overfitting. Another subjective quantification treats the evolution of the IC/DV peak and valley as indicative of degradation modes. Seo et al. employed this approach to identify degradation in high-rate cycling batteries, but it did not exhibit robust generalizability [19]. In addition, EIS links changes in impedance within a specified frequency range to the electrical components of an equivalent circuit model, correlating them with the most relevant modes [20]. The DTV incorporates entropy heat generation information into battery phase transition processes and attempts to achieve quantification [21, 22]. However, both methods require additional testing tailored to the specific device, posing data acquisition challenges and complicating the practical implementation of this method.

The fitting of ICs has been widely applied to degradation mode identification. Dubarry et al. proposed the peak-valley features of IC/DV curves for fitting rather than all values [23]. Nevertheless, traditional quantification often requires tedious and time-consuming manual trials. Machine learning has overcome the bottlenecks of noninvasive degradation diagnosis. Extensive research has been conducted on ML-based automatic IC fitting and aging identification using a mechanistic model to generate synthetic data. Dubarry et al. pioneered the establishment of a comprehensive big data dataset covering extensive paths of test batteries using half-cell experimental data, marking the advent of artificial intelligence algorithms for battery diagnosis and prognosis [24, 25]. Previous studies have validated the feasibility of data-driven degradation diagnosis using these publicly available datasets [26-29]. Costa et al. [30] transformed IC sequences into images and applied convolutional neural networks (CNNs) to validate hypothetical synthetic batteries. Additionally, the aging conditions of datasets have been further extended to photovoltaic charging [31]. While synthetic data prevent the need for experiments and highlight the potential for diagnosing real batteries, most studies lack persuasive validation based on cycling tests. Thelen et al. [32] proposed data augmentation and delta learning for diagnosing cells and validated this approach through a comparison with manually fitted experimental DV curves. Data-driven identification can be improved through features and algorithms [33, 34].

While the data-driven methods optimally perform with access to the automatic identification of degradation, accurate diagnosis always requires rigorous testing involving extremely low current rates and complete charge/discharge cycles. In previous research, diagnosing the degradation modes through IC/DV fitting depended on reference performance tests specifically conducted during the experimental procedures, which required C/20 charge/discharge or even lower [30, 32, 35]. Thus, additional diagnostic tests in practice are needed, and due to deviations from normal usage, regular calibration is also needed. Moreover, the accuracy of these methods encounters typical challenges when the interdependence of different modes makes reliable degradation diagnosis difficult. To improve the diagnostic performance, Li et al. [36] performed multistep identification based on the sensitivity of VQ reconstruction and ECM parameters, and Kim et al. [35] applied the classification to credibly reveal the distinct effects of LLI and LAM, making the preclassification or stepwise diagnosis approach a potentially viable way to address this difficulty.

In conclusion, systematic and effective methods for diagnosing battery degradation with good practicality are lacking. To address these challenges, an innovative battery degradation diagnosis framework is proposed in this study, which makes the following contributions. First, by leveraging mechanistic models for synthetic dataset generation, a Gaussian process regression (GPR) model is constructed by correlating the IC sequences and battery aging evolution for the estimation of SOH and degradation modes. The training dataset does not rely on any historical calibration data, thus overcoming the limitations of the sparse set of experiments. Second, a multistep diagnosis strategy is developed to handle the complex coupling of different degradation modes on charging data. This method analyses the sensitivity of VQ responses to different modes and then sequentially quantifies them. The overpotential correction addresses higher current rates by subtracting the voltage offset. The effectiveness of the proposed framework was validated through experiments on 6 cells under different operating conditions. Through synthetic data, the SOH can be accurately estimated to within a 2% RMSE, and the degradation modes can be accurately diagnosed with an error within 1.5% under a loaded current up to C/4. This signifies a meaningful improvement in that degradation diagnosis can be applied under normal usage.

The remainder of this paper is structured as follows: Section 2 introduces the batteries and the experimental procedures. Section 3 provides a brief overview of the degradation modes and mechanism models, while Section 4 discusses the structure and principles of the degradation diagnosis framework. Section 5 analyses the aging of the experimental batteries and presents the diagnostic results of the SOH and degradation modes considering voltage windows and different rates. Finally, Section 6 concludes the paper.

2. Experiments

The experimental data used in this study were sourced from publicly available experimental datasets provided by the Technical University of Munich (https://doi.org/10.14459/2022mp1690455). The comprehensive procedure for assessing battery and electrode characteristics under varying cycling conditions has been detailed elsewhere [16]. Consequently, in this section, the fundamental battery information and the experiment employed in our research are concisely summarized.

For this study, the commercial INR18650-MJ1 battery manufactured by LG was used. The manufacturer stipulated the minimum standard capacity as 3.35 Ah, which formed the basis for the C-rates used in the experiments. A charge of double the nominal capacity (6.7 Ah) is defined as an equivalent full cycle (EFC). The battery employs a nickel-rich NMC-811 positive electrode and a combination of graphite and silicon as the negative electrode material. Thorough characterization and cycling tests were conducted on the battery using the CTS battery testing system from BaAyTec within a controlled environment at a constant temperature of 25°C. Table 1 summarizes the experimental procedures conducted on the 6 examined cells. These procedures included a continuous 486-day aging test sequence followed by an expanded charging rate test after 158 days of rest.

Aging Test Sequence. Each sequence began with capacity and pulse tests to gather basic battery information. Subsequently, application phase tests simulating real-life operations were performed but not extensively studied. Charging rate tests were conducted to acquire constant current-constant voltage responses at different rates (C/30, 0.264C, 0.5C, and 1C) and a constant power constant voltage (3.183 W) charging response within the voltage range of 2.5-4.2 V. During the continuous cycling phase, the 6 cells were divided into three groups and cycled in different voltage ranges, labelled Conditions I-III in Table 1.

Extended Rates Test. Extended tests at various rates were necessary for determining the rate requirements for the charging curves used in diagnosis. After the aging test sequence, charging tests were conducted at rates of 0.264 C, C/6, C/8, C/10, C/12, C/15, C/20, C/25, and C/30. Between these stages, a constant discharge at 0.2 C to 2.5 V was applied. The extended rate tests were conducted on two cells under Condition II.

The half-cell characteristic test stemmed from the assembly of coin cells after opening the full cell in the argon-filled glovebox; the detailed operations are provided in Ref [37]. This research shares the obtainable data from the experiments detailed earlier. These data specify that the voltage range of the VQ curve spans from 3.0 V to 4.2 V, with the capacity defined by C/30 charging within this range. In practical use, the cell ceases to be of use when its SOH deteriorates to less than 80%, which is defined as the end of life (EOL). Therefore, our research primarily focused on the data where the SOH remained above 80%.

Table 1 Experimental procedures applied to the individual cells. N_{test} is the number of iterations of the aging test sequence applied to an individual cell.

Cell No.	Aging Condition	Cell test type	Experimental Procedures: Aging test sequence	Experimental Procedures: Extended rates test	N_{test}
#73	Condition I: 2.5 V-4.2 V	I-1	✔	✘	11
#86		I-2	✔	✘	11
#75	Condition II: 3.6 V-4.2 V	II-1	✔	✔	24
#76		II-2	✔	✔	26
#85	Condition III: 2.5 V-4.0 V	III-1	✔	✘	26
#78		III-2	✔	✘	26

3. Mechanistic model-based degradation mode identification

3.1 Mechanistic model construction

Degradation modes reduce the complexity of the aging mechanism and facilitate quantitative analysis. These modes include three modes, as illustrated in Fig. 1: LLI represents the consumption of available lithium, and LAM_{PE} and LAM_{NE} represent the failure of electrode active materials [17]. Detailed information on the typical degradation modes is provided in Appendix A. Note that in this study, without specific clarifications, the VQ curves were obtained at a low current rate. Previous studies [13, 38-41] have developed equations and models in which the full-cell VQ curve is considered to match the OCPs of the positive and negative electrodes after shifting and scaling. The unique effects of different aging modes on the VQ are mapped to the electrode OCP curves. The mechanistic model was constructed based on the OCPs, enabling the noninvasive analysis and prognosis of battery degradation without complex sensors or high computational costs. This approach ignores the influences of kinetic effects and assumes that the shape of the half-cell OCP remains stable during aging.

The full-cell VQ (U_f) is defined as the difference between electrode OCPs (U_p and U_n), with the half-cell OCP curve as a function of the electrode SOC (SOC_p and SOC_n) [38-41]:

$$U_f = U_p(SOC_p) - U_n(SOC_n). \tag{1}$$

The mechanistic model suggests that due to the uncertain capacity loss in the negative electrode, employing the SOC scale on the positive electrode as a reference for calculating the battery SOC is sensible [13]:

$$U_n = f(SOC_p). \tag{2}$$

Hence, a relationship exists between the SOC of the positive and negative electrodes:

$$SOC_n = (1 - SOC_p). \tag{3}$$

Parameterizing the shifting and scaling in OCP curve matching is crucial [13, 16]: the movement of the OCPs for the positive and negative electrodes x_{offset} is used for shifting, and the positive and negative electrode capacity ratio CR is used for scaling, which is defined as follows:

$$CR = \frac{Q_n}{Q_f}. \tag{4}$$

The initial CR_0 is adjusted considering the shifting parameter $x_{\text{offset-fresh}}$:

$$CR_{\text{fresh}} = (1 - x_{\text{offset-fresh}})CR_0. \tag{5}$$

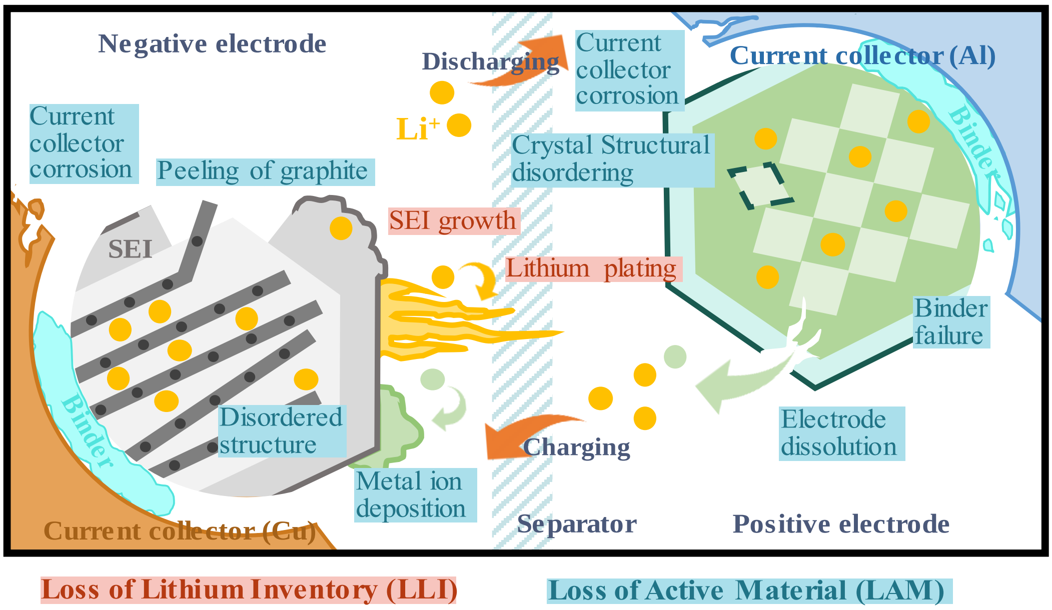

Fig. 1. Schematic of degradation mechanisms and associated degradation modes in a lithium-ion battery.

The initial offset $x_{\text{offset-fresh}}$ represents the VQ response when the SEI film is formed, simulating negative electrode loss during battery manufacturing. Thus, Eq. (4) can be rewritten as:

$$SOC_n = (1 - SOC_p)CR_{\text{fresh}} + x_{\text{offset-fresh}}. \tag{6}$$

As previously mentioned, quantifying the impact of modes on VQ changes can successfully shift the focus towards the effects of the shifting parameter $x_{\text{offset-fresh}}$ and the scaling parameter CR_{fresh}.

LAM affects the lithiation/delithiation process of the electrodes, reducing the range of the OCP on the SOC_p scale, i.e.,

$$CR_{\text{aged}} = CR_{\text{fresh}}\left(\frac{1 - LAM_{NE}}{1 - LAM_{PE}}\right). \tag{7}$$

$$x_{\text{offset-aged}} = x_{\text{offset-fresh}} + \frac{CR_{\text{aged}}}{CR_{\text{fresh}}} \times LAM_{PE}. \tag{8}$$

LLI does not directly impact the electrode response. However, due to cumulative losses, the reduced active lithium embedded in the negative electrode during cycling alters the shifting parameter $x_{\text{offset-fresh}}$ between electrodes, as shown in Eq. (9).

$$x_{\text{offset-aged}} = x_{\text{offset-fresh}} + \frac{CR_{\text{aged}}}{CR_{\text{fresh}}} \times LAM_{PE} + LLI. \tag{9}$$

Fig. 2 demonstrates the successful VQ and DV matching of the half-cell curves with those of fresh experimental cells. This approach requires the shifting parameter $x_{\text{offset-fresh}}$ to be determined based on the initial voltage of the fresh cell VQ curve and the scaling parameter CR to be subsequently adjusted through analyses of the VQ and DV curve shapes and final voltage. Following a comparative fitting, the capacity ratio CR was set at 0.9, and the offset x_{offset} was set at 14%. Extensive applications of the mechanistic model have established a theoretical background for diagnosing and predicting degradation [24, 30, 33, 35].

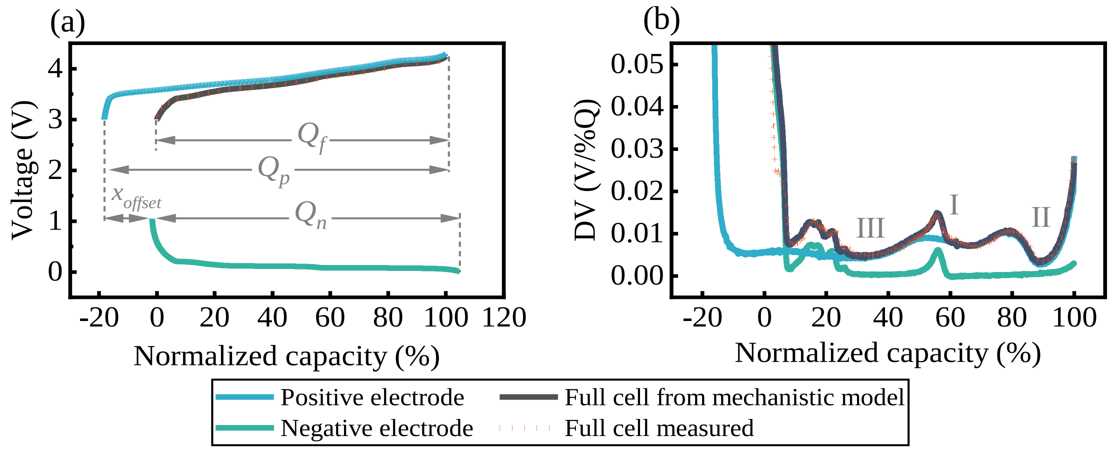

Fig. 2. The comparison between the simulation of half-cell matching based on mechanistic models and the C/30 charging of a fresh battery. (a)VQ; (b)DV.

3.2 Degradation mode identification and synthetic dataset

Preassigning the degradation mode effects to the shifting parameter $x_{\text{offset-fresh}}$ and scaling parameter CR enables the degradation to be quantified. Throughout this process, the initial parameters set in Section 3.2 serve as the reference for matching the half-cell OCP curve of a fresh battery. The three different modes, LLI, LAM_{PE} and LAM_{NE}, are adjusted to achieve a match between the experimental VQ and DV and the simulated curves altered by the mechanistic model. Cells with varying degrees of degradation are expected to exhibit different characteristics. The manually fitted quantified values of the modes are assumed to be the 'true' LLI, LAM_{PE}, and LAM_{NE} values. These findings serve as a reference for the results of the diagnostic framework proposed in this study.

Manual fitting employs prior knowledge about the characteristics of experimental cells to prevent illogical results from developing during the matching process. The changes in the peaks and valleys of the IC/DV are crucial for analyzing the battery degradation of various materials. For different chemistries, finding corresponding specific changes in peaks and valleys enables the identification of degradation modes [42]. The peaks and valleys of the DV curves, marked as I-III in Fig. 3b, are more easily recognizable and utilized to quantify degradation modes than those of the VQ curves. Moreover, compared with the IC curves, the DV curve is a derivative with respect to capacity, and the shifts in the DV peaks and valleys are dominated by the capacity loss, which improves the accuracy of the manual degradation mode quantification for the reference values. For precise matching, we modify the LLI, LAM_{PE}, and LAM_{NE} as follows:

Step 1: Targeting the experimental curve for quantification, LLI is adjusted based on Valley II of DV. For the tested batteries, the negative electrode is limiting at the end of discharge, and the positive electrode is limiting at the end of charge, so the capacity loss is usually proportional to the LLI [42]. Due to the high correlation between the LLI and capacity loss, Valley II exhibits a leftward shift.

Step 2: Peak I represents the phase transition of the electrode materials of the experimental battery. As LLI barely affects this transition, Peak I is influenced mainly by LAM during degradation. Therefore, LAM_{PE} and LAM_{NE} are adjusted based on the initial and final voltages and the movement of Peak I, respectively.

Step 3: Steps 1 and 2 are repeated until logical and precise curve fitting results are obtained, yielding the most appropriate modes.

Through manual fitting, we individually analyzed each of the 6 cells tested in the experiment. The cells cycling across the three different voltage windows showed typical degradation pathways. In Section 5.1, the quantification used to evaluate the rationality of the results is assessed, and aging is summarized. If the curve fitting for obtaining numerical degradation values is considered a forwards process, the creation of a synthetic dataset corresponds to its inverse process, which was inspired by previous research [24, 25, 32, 35]. Through the mechanistic model, which acts as a digital twin of an actual battery, any assumed combination of degradation modes yields the full-cell VQ curve. The differentiation functions DV and IC are derived in the dataset setup. The more enriched the path setup is, the more it tends to encompass the actual battery aging paths. First, by setting different combinations of degradation modes, a three-dimensional cube is established for full coverage, where LLI, LAM_{PE}, and LAM_{NE} constitute its three dimensions. After this phase, these combinations are processed through the mechanistic model to obtain VQ curves composing the synthetic dataset. Finally, the scaling down in VQ represents the span change pointing towards the capacity loss. The VQ curves are subsequently differentiated on the capacity scale and the voltage scale. This process is performed in MATLAB to generate artificial data and establish a dataset for analysis and machine learning.

4. Methodology

4.1 Degradation diagnosis framework

The diagnostic framework for capacity loss and degradation modes have several components, including data generation, training and diagnosis results based on multistep diagnosis. Fig. 3 shows the details of every module. Data generation provides the foundation for training the dataset within the framework. During training, GPR is utilized to establish a map between effective IC sequences and the combination of the SOH and the degradation modes. The model is then used on the experimental cells, considering common voltage windows and higher test rates. This framework introduces a multistep diagnosis method to navigate the challenges encountered in degradation mode identification. This framework incorporates mechanistic models and machine learning while conducting an incremental capacity analysis under stronger usability conditions.

Data generation. This module was employed to generate a comprehensive synthetic dataset for diagnosis. The principles behind synthetic data generation are outlined in Section 3.3. Within the MATLAB coding environment, the testing data from C/30 were used to establish a mechanistic model of the experimental cells and to determine the degradation modes for constructing the synthetic dataset. To facilitate efficient degradation diagnosis and limit the computational overhead, the upper limits for LLI and LAM_{NE} were set at 20%, while LAM_{PE} was capped at 10%. This setup acknowledges the predominant influences of LLI and LAM_{NE} in the aging process of 18650 nickel-rich silicon-graphite lithium-ion batteries, with infrequent occurrences of LAM_{PE}, as supported by a wealth of research [16]. The various combinations of degradation modes, including VQ and capacity loss, yielded 4851 corresponding datasets, indicating low computational complexity and high suitability for machine learning.

Training. ICA is a crucial element for comprehending cell performance and degradation, as well as a pivotal input for machine learning. The IC sequences derived from synthetic VQ curves were utilized as feature inputs for multiple reasons. First, the DV data were affected by capacity loss, but the IC sequence values were extracted from a stable voltage window, which can be readily obtained during offline testing. Furthermore, in contrast to the peak-valley features of the IC, the full sequences can address the potential issue where these peak valleys might diminish during aging. An appropriate voltage interval must be selected during the extraction of incremental capacity sequences. A smaller interval introduces considerable noise, which makes identifying curve features such as peaks and valleys challenging. Conversely, a larger interval provides a smoother curve but results in the loss of most features. Following careful evaluation, a 4 mV voltage interval was deemed optimal for combining feature retention with curve smoothness and it is suitable for machine learning inputs. Unlike deep learning, which requires vast amounts of data, common machine learning methods exhibit task feasibility and lightweight implementation [32]. GPR was chosen for machine learning within the diagnosis framework due to its flexibility in handling nonlinear and high-dimensional issues without assuming target functions. The model uses inputs of the IC sequences and outputs of the SOH along with degradation modes.

Diagnosis Results. The model developed through machine learning was applied to acquire diagnostic results of experimental cell degradation data. Generally, the IC sequences were extracted from the VQ curves of C/30 charging rate tests within the voltage range of 3.5 V - 4.2 V. The C/30 test offers more stability without kinetic factor interference. Moreover, the 3.5 V-4.2 V voltage window covers almost all the IC characteristics and approximately corresponds to 15%-100% of the SOC. Nevertheless, practically obtaining such low rates and wide windows is challenging because cells are rarely discharged entirely during operation. Hence, common voltage windows and higher charging rates are the focus of this analysis. For higher rates, a simple voltage compensation that involves subtracting a constant voltage addresses the IC deviation to allow higher rate curves for diagnosis.

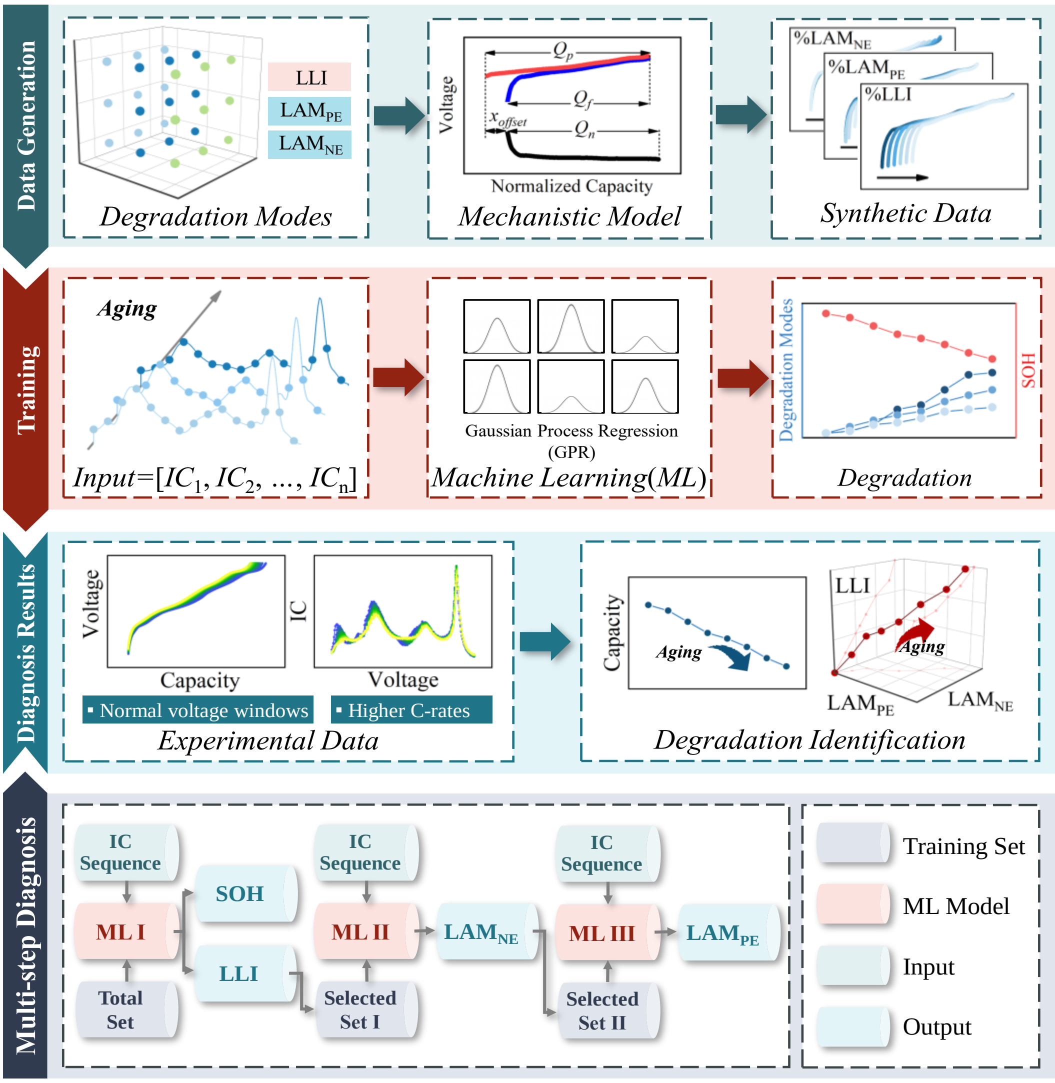

Fig. 3. Diagnosis framework for SOH estimation and degradation modes identification.

To confirm the degradation modes, in this framework, a multistep diagnosis method that considers the multiple effects of modes is proposed. Different mechanisms interconnect to influence battery characteristics; thus, the trigger for changing IC sequences is the combined action of the LLI and LAM. Synthetic data from mechanistic models eliminate the need for additional experiments while establishing datasets. An arbitrary combination of degradation modes covers many possible aging paths and corresponds to IC sequences. However, when machine learning analyses the influence of modes on IC sequences through mapping relationships, single-step methods encounter challenges when confirming interacting degradation modes, as well as disparities between field data and synthetic data. As a result, multistep diagnosis incorporates the sensitivities of different degradation modes as inputs to systematically identify these modes.

The procedure for achieving more precise and reliable quantification involves three steps. Each step is matched to a machine learning model. In the first step, the machine learning model *ML I* was trained by using the entire synthetic dataset *Total Set* to estimate the SOH and LLI. They exhibited greater sensitivity to IC changes than did the LAMs because their variations directly led to shifts and scales in the VQ curve. The initial delay in the capacity loss effects of LAM_{PE} and LAM_{NE} produced slight changes in IC features[43]. Therefore, the diagnosis first focuses on SOH estimation and LLI identification. In the second step, the identified LLI was used to establish the *Selected Set I* for training *ML II*. Assuming the identified LLI is *x*, *Selected Set I* comes from the portion where LLI is [*x*] and [*x*]+1 ([*x*] represents the integer value of *x*) of the *Total Set*, which limits the range of LLI. Compared to *Total Set*, this rule largely eliminates the impact of LLI on IC sequences and enables more robust quantification of LAM_{NE} based on *ML II*. In the third step, the training set *Selected Set II* was built with the same logic. Assuming that the recognized LAM_{NE} is y, *Selected Set II* is filtered from *Selected Set I* to satisfy [*y*] and [*y*]+1. *ML III* is subsequently employed to identify LAM_{PE} after the influence of LAM_{NE} is mitigated. Multistep diagnosis aids in the incremental identification of degradation modes, enabling the specific battery aging trajectory to be precisely estimated.

4.2 Gaussian progress regression

Gaussian process regression, a computationally efficient traditional machine learning method, is employed to learn the mapping between IC sequences and SOH as well as degradation modes. The training set consists of inputs $\boldsymbol{X} = [\boldsymbol{x_1}, \cdots, \boldsymbol{x_n}]^{\mathrm{T}}$ and outputs $\boldsymbol{Y} = [\boldsymbol{y_1}, \cdots, \boldsymbol{y_n}]^{\mathrm{T}}$, where GPR assumes $y_i = f(\boldsymbol{x_i}) + \varepsilon_i(\varepsilon_i \sim N(0, \sigma_n^2))$, and the model is trained accordingly. The output is defined to follow a mean function $m(\boldsymbol{X}) = 0$ and a covariance function $\boldsymbol{K}$ ($\boldsymbol{K_{ij}} = k(\boldsymbol{x_i}, \boldsymbol{x_j})$):

$$\boldsymbol{Y} \sim GP(0, \boldsymbol{K}(\boldsymbol{X}, \boldsymbol{X}) + \sigma_n^2). \tag{10}$$

For a given input $\boldsymbol{x}^*$, the distribution between the training set and the predicted output y^* satisfies:

$$\begin{bmatrix} \boldsymbol{Y} \\ y^* \end{bmatrix} \sim GP\left(\boldsymbol{0}, \begin{bmatrix} \boldsymbol{K}(\boldsymbol{X}, \boldsymbol{X}) + \sigma_n^2 \boldsymbol{I_n} & \boldsymbol{K}(\boldsymbol{X}, \boldsymbol{x}^*) \\ \boldsymbol{K}(\boldsymbol{x}^*, \boldsymbol{X}) & k(\boldsymbol{x}^*, \boldsymbol{x}^*) \end{bmatrix}\right). \tag{11}$$

Here, $\boldsymbol{I_n}$ is the identity matrix. The expectation and variance of y^* come from the conditional distribution probability of the training set:

$$m^* = k(\boldsymbol{x}^*, \boldsymbol{X})[\boldsymbol{K}(\boldsymbol{X}, \boldsymbol{X}) + \sigma_n^2 \boldsymbol{I_n}]^{-1} \boldsymbol{Y}, \tag{12}$$

$$\sigma^{*2} = k(\boldsymbol{x}^*, \boldsymbol{x}^*) - \boldsymbol{K}(\boldsymbol{x}^*, \boldsymbol{X})[\boldsymbol{K}(\boldsymbol{X}, \boldsymbol{X}) + \sigma_n^2 \boldsymbol{I_n}]^{-1} \boldsymbol{K}(\boldsymbol{X}, \boldsymbol{x}^*). \tag{13}$$

The covariance function describes the spatial central distance between two variables and represents the correlation between them. For simplicity, the Matérn covariance function is adopted in this study:

$$k_{Matérn}(\boldsymbol{x_i}, \boldsymbol{x_j}) = \sigma_f^2 \frac{2^{1-\nu}}{\boldsymbol{\Gamma}(\nu)} \left(\frac{\sqrt{2\nu}\|\boldsymbol{x_i} - \boldsymbol{x_j}\|}{l}\right)^{\nu} \boldsymbol{K_\nu}\left(\frac{\sqrt{2\nu}\|\boldsymbol{x_i} - \boldsymbol{x_j}\|}{l}\right). \tag{14}$$

Here, σ_f^2 is the sample signal variance, $\|\boldsymbol{x_i} - \boldsymbol{x_j}\|$ is the distance between input points, ν is the smoothness parameter, l is the scale parameter, $\boldsymbol{\Gamma}(\cdot)$ is the gamma function, and $\boldsymbol{K_\nu}(\cdot)$ is the modified Bessel function. ν can be chosen based on the dataset, such as 0.5 or another value. The hyperparameter $\boldsymbol{\theta} = \{\sigma_f, \sigma_n, l\}$ is obtained by minimizing the negative log marginal likelihood $NLML = -\log(\boldsymbol{Y}|\boldsymbol{X}, \boldsymbol{\theta})$.

Additionally, the estimated SOH values can be compared with the actual measurement values using the root mean square error (RMSE):

$$RMSE = \sqrt{\frac{1}{n}\sum_{i=1}^{n}(y_i - \hat{y}_i)^2}, \tag{15}$$

where y_i is the observation, $\hat{y}_i$ is the estimation, and n is the total number of test samples. The degradation modes are expressed by the absolute value of the error $|y_i - \hat{y}_i|$, which represents the difference from the fitted reference values.

5. Results and discussion

5.1 Model fitting and degradation analysis

In this section, the tested cell degradation based on manually fitting results from the capacity loss and DV curves, which are detailed in Appendix B, is presented and analyzed.

The SOH based on capacity is considered the variable for charge throughput during testing. Fig. B.1 delineates the SOH of cells under each aging condition. Throughout the tests, all the cells underwent significant degradation. Consistency in degradation was observed between cells under identical conditions, whereas the degradation rates varied under differing conditions. Cells cycling over the full voltage range in Condition I (2.5 V-4.2 V) experienced faster degradation. The SOH decreased to 80% after approximately 570 EFC, which is only half of that of Condition II (3.6 V-4.2 V) and Condition III (2.5 V-4.0 V). Jung et al. [44] characterized conditions where the upper cutoff voltage exceeded 4.0 V as indicative of electrode material instability, causing accelerated degradation across the full voltage range. Additionally, Schindler et al. [45] suggested that limiting the upper cutoff voltage could alleviate the degradation of positive and negative electrode materials, extending the cycle life.

The tests at a C/30 charging rate were denoted as T1-Tn. The DV curves were manually fit through a mechanistic model for three-phase diagnosis (initial, intermediate, and final tests during the aging sequence), as depicted in Fig. B.2. Considering the consistency among identical model cells under the same conditions, specific cells were selected for detailed analysis of each condition. For Condition II-1, the initial test T1 (see Fig. B.2 (d)) reveals perfect agreement between the fresh cell and the simulation. No signs of degradation were present at this stage. However, during the intermediate test T12, minor degradation modes were identified in the fitting: 6.1% LLI, 1.9% LAM_{PE}, and 6.3% LAM_{NE}, with SOH decreasing to 92.5%. In the final test, T24, the cells exhibited sustained aging and more evident modes. The fitting is illustrated in Fig. B.2 (f), where the deviation between the simulation and testing results is attributed to the disappearance of Peak I in the curve. During aging, the shape of the DV curve greatly changes. Valley II notably shifted to the left due to the curve reduction caused by capacity loss at the normalized capacity scale. This shift primarily indicates lithium-ion failure caused by the strong correlation between the LLI and SOH. Additionally, Peak I decreased while shifting, which may be due to the gradually diminishing contribution of silicon [46].

Fitting was applied to all tests to extract the degradation modes for each cell. The corresponding paths are illustrated in Fig. B.3. The optimization for VQ reconstruction in Ref [16] revealed degradation modes with consistent trends and scales that exhibit minor discrepancies due to methodological variations. Cells subjected to identical conditions exhibited similar outcomes. Analogous to SOH, aging accelerated within the full voltage range in Condition I. Across all the experiments, LLI and LAM_{NE} were the major contributors to degradation, a perspective substantiated by existing research [47, 48]. Notably, the mechanistic model applied the pristine negative composite electrode OCP from the fresh half-cell and thus did not differentiate the different losses of graphite and silicon, which slightly compromised the diagnostic results [48].

Theoretically, constructing the half-cell curves of the blended negative electrodes with consideration of the contributions of silicon can provide more accurate results for diagnosis because silicon particles undergo greater aging during cycling than graphite particles, i.e., $LAM_{NE\text{-}Gr}$ for graphite and $LAM_{NE\text{-}Si}$ for silicon; this potentially is caused by the more severe volumetric change in silicon and the greater current density [49-51]. However, incorporating silicon degradation into the changes of the negative electrode half-cell requires the introduction of new aging dimensions, thus increasing the complexity of ML modeling; additionally, the electrochemical activity features of silicon in the low-voltage and low-SOC windows of IC and DV curves cause challenges for efficient and rapid diagnosis using partial charge data in practice [47, 52]. The use of fixed negative electrode half-cell curves for degradation diagnosis has been widely adopted [16, 47, 53], with the quantified LAM_{NE} mainly reflecting the loss of graphite that generally accounts for more than 90% of the content of the negative electrode material. Anyhow, it is acknowledged that the electrode losses of silicon and graphite were not distinguished, which potentially compromises the results of the LAM_{NE} diagnosis. The detailed analysis is provided in Appendix C.

In conclusion, the mechanistic model based on the pristine negative composite electrode provides an effective aging analysis method for nickel-rich silicon-graphite batteries. The degradation modes quantified using DV curves provide a valuable reference for the diagnostic framework.

5.2 Battery aging diagnosis based on the multistep diagnosis framework

In this section, the proposed diagnosis framework is applied to SOH and degradation acquisition of test curves under a wide voltage window at low rates. In this section, low rates have charging currents of C/30. The wide window spans a voltage range of 3.5 V to 4.2 V, which captures nearly all pertinent information within the charging curve and corresponds to approximately 15% to 100% of the SOC window. These test data are derived from a controlled laboratory environment and enable the capacity and degradation modes to be assessed.

When estimating SOH, the machine learning model computes the relationship between IC sequences within a certain voltage range and SOH. This model uses synthetic data generated by MATLAB for rapid and simple simulation, but it lacks real-cell information. Even though the synthetic data are derived from the mechanistic model, which is a digital twin of a real cell, the model encounters challenges in providing comprehensive operational details. To address this, the training dataset was augmented by incorporating experimental data into the synthetic data, denoted as SIM+EXPN. Table 1 shows the iteration count for each cell in the aging test sequence. Thus, the SIM contains the simulated data, while EXPN contains the C/30 charging from the charge rate test in the first N tests from the aging test sequence. The augmented data are labelled EXP1-EXP5 and represent the early cycle data, approximately equivalent to 200 EFCs based on charge throughput. Furthermore, data augmentation was performed separately for the cells based on their respective operational conditions.

The RMSE values for SOH estimation are presented in Fig. 4. Each subplot represents the SOH estimation model augmented with limited experimental data from one of the three conditions (Figs. 4(a)-4(c)) or all conditions together (Fig. 4(d)). Moreover, each subplot verifies the performance using the cells under the three operating conditions; thus, the horizontal axis of each subplot is labelled I-III. The vertical axis shows the augmented training datasets containing different amounts of experimental data. Darker shades indicate higher RMSEs and lower accuracies. The accuracies of the models varied under different conditions. For each subplot, two cells from Condition I degraded the fastest and exhibited notably lower predictive accuracy than did the other 4 cells. This disparity might be due to the limited dataset available for estimation caused by rapid aging, which resulted in unreliable RMSEs: each cell in Condition I underwent only 11 tests for SOH estimation. Moreover, rapid degradation might cause a discrepancy between synthetic and experimental data in terms of the relationship between IC sequences and SOH, which highlights the importance of augmenting the data with experimental results. SIM+EXP0 represents the model trained only with synthetic data, which roughly captures the SOH degradation of the experimental cells. SIM+EXP1 to SIM+EXP5 demonstrate that the diagnostic framework performance in estimating SOH is enhanced by adding pairs of experimental IC sequences and SOH to the training set. As shown in Figs. 4(a)-4(c), incorporating experimental data from each operational condition improves the prediction accuracies of the models and benefits other cells. Fig. 4(d) displays the cumulative effect of adding early-stage data from all conditions to the training set when distinguishing conditions. Data augmentation reduces the gap between the mechanistic model and real cells, enhancing estimation accuracy. The performance stabilizes as the quantity of experimental data increases. The SOH estimation module can be corrected and improved using minimal data.

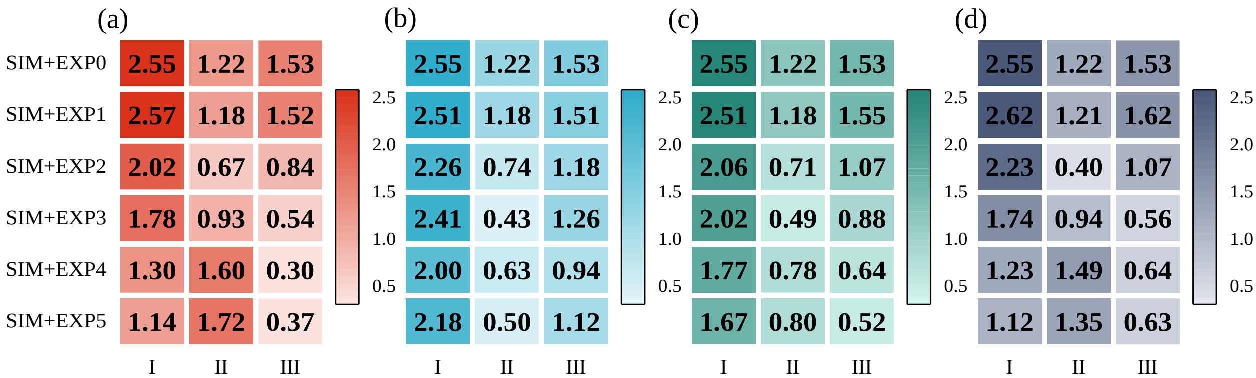

Fig. 4. RMSE values in battery SOH estimation for the cells under the three operating conditions, labelled as I-III. Each subplot represents the SOH estimation model augmented with limited experimental data from one of the different conditions: Condition I (a); Condition II (b); Condition III (c); and from all conditions together (d).

The diagnostic framework was employed for both SOH estimation and degradation mode identification. Figs. 5(a)-5(c) show the identification of Condition II-1, which is representative of 6 cells. In comparison to the results obtained from previous models, the multistep diagnosis successfully identified LLI, LAM_{PE} and LAM_{NE}. The single-step direct identification of the degradation modes using the applied algorithm in the framework was be challenging, as shown in Figs. 5(a)-5(c). The mutual coupling effect of the degradation modes on the VQ curve caused difficulty in the extraction of the modes using the IC sequences within the dataset. Therefore, a multistep diagnosis combined with Gaussian process regression was used to improve the degradation diagnosis. It first identified easily discernible high-sensitivity modes such as LLI and acquired the corresponding datasets, mitigating the influence of LLI on machine learning identification. This principle was also applicable to LAM_{PE}. Figs. 5(d)-5(e) show the absolute errors of LAM identification relative to the reference under the proposed framework and without it. For Conditions II and III, the upper quartile of diagnostic bias according to the proposed framework remains within 1.5%, with Condition III-1 exhibited broader dispersion, likely due to battery uniqueness. The LAM_{NE} values of the two cells in Condition I appear to differ from our expectations. Akin to SOH estimation, the underlying reasons for this difference include insufficient data volume and rapid degradation. Notably, the LLI did not provide a highly accurate reference for the LAM_{NE} dataset. In summary, multistep diagnosis yields a median error distribution within 2%, confirming the successful diagnosis of degradation modes and the applicability of this approach to various aging scenarios.

5.3 Battery aging diagnosis based on the common charging voltage window

In this section, the SOH estimation accuracy when using IC sequences within a common voltage window is analyzed. This entails utilizing a narrower range, which includes only a segment of charging curves for diagnostics rather than the complete set. This eliminates the need for full charging protocols and reduces the testing time, but it also influences diagnosis and leads to a lack of training features. Hence, the proposed diagnosis framework employs a selected common voltage window for SOH estimation and degradation mode identification, aiming to achieve a meaningful balance between portability and accuracy.

Fig. 6 presents the RMSE values of the SOH estimation for representative Condition II in different voltage windows. The horizontal axis of each plot represents the starting voltage ($Voltage_{min}$) of the voltage window, while the vertical axis indicates the ending voltage ($Voltage_{max}$). Each rectangle corresponds to a specific window, with colors indicating the RMSE—red for high accuracy and blue for lower accuracy. As depicted in Fig. 6(a), the precision of SOH estimation is critically influenced by the chosen voltage window. However, this does not imply that IC sequence values from the entire window perform better. The inclusion of the low-voltage portion (notably from 3.1 V to 3.3 V and even 3.4 V) does not yield significant fluctuations during aging, thus providing information that is ineffective for diagnosis while increasing the number of input dimensions that interfere with machine learning. This is why we selected the window of 3.5 V-4.2 V in Section 5.2. Beyond the $Voltage_{min}$ requirement, a portion of the voltage window should include a $Voltage_{max}$ of at least 4.1 V for effective SOH estimation. Features at approximately 4.1 V in the IC sequence roughly correspond to Valley III in the DV curve, representing a phase transition in NMC-811, which is a distinctive characteristic of its positive electrode material [54]. Experimental data augmentation is also considered, and Figs. 6(b)-6(c) shows the SOH estimates after different amounts of early data are incorporated. As in Fig. 4, augmentation enhances the accuracy and

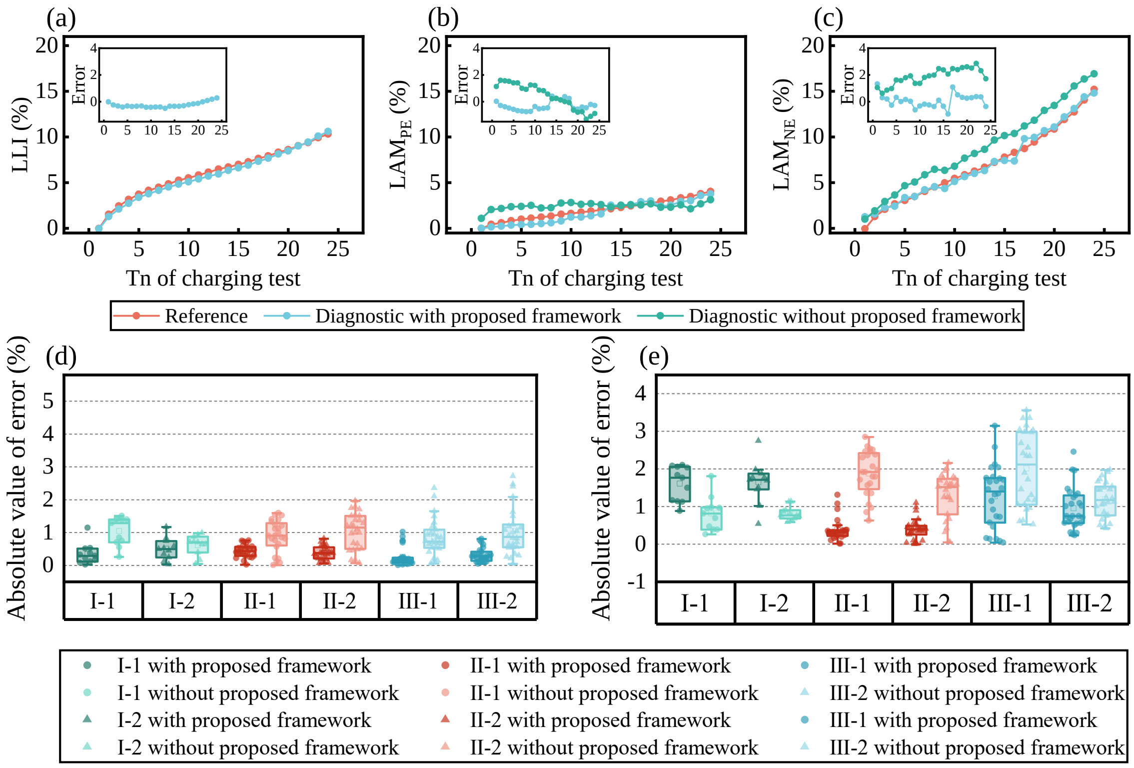

Fig. 5. Degradation modes diagnostics with and without the proposed framework for cell#75 (Condition II-1): (a) LLI; (b) LAM_{PE}; (c) LAM_{NE}. Tn denotes the n^{th} one of the C/30 rate charging tests. The absolute value of the error with and without the framework for batteries under different aging condition: (d) LAM_{PE}; (e) LAM_{NE}.

improves the performance of the voltage range rectangles, which perform poorly when composed solely of simulated data. Following analysis and comparison, an IC sequence voltage window of 3.6 V-4.1 V is chosen for diagnosis. This window should be concurrently applicable to degradation modes.

In Fig. 7, two common voltage windows are used for degradation mode acquisition: 3.6 V-4.1 V and 3.8 V-4.1 V. The former demonstrated excellent performance in SOH estimation, while the latter adopted a narrower voltage window within acceptable estimation limits. Figs. 7(a)-(c) showcase the results obtained using the IC sequences within the common voltage window of 3.6 V-4.1 V, enabling aging analysis with partial charge data. The diagnosed modes exhibited overall error values within 2% compared to the reference, albeit slightly larger than the wide voltage window. Nonetheless, this approach reduces the time required to obtain IC sequences in practical applications. The sequences within 3.6 V-4.1 V encompass all the response information necessary for both SOH estimation and degradation mode identification. Figs. 7(d)-7(f) depict the diagnosis within 3.8 V-4.1 V, revealing significant errors that render it unsuitable for diagnosis. The range of 3.6 V-3.8 V roughly

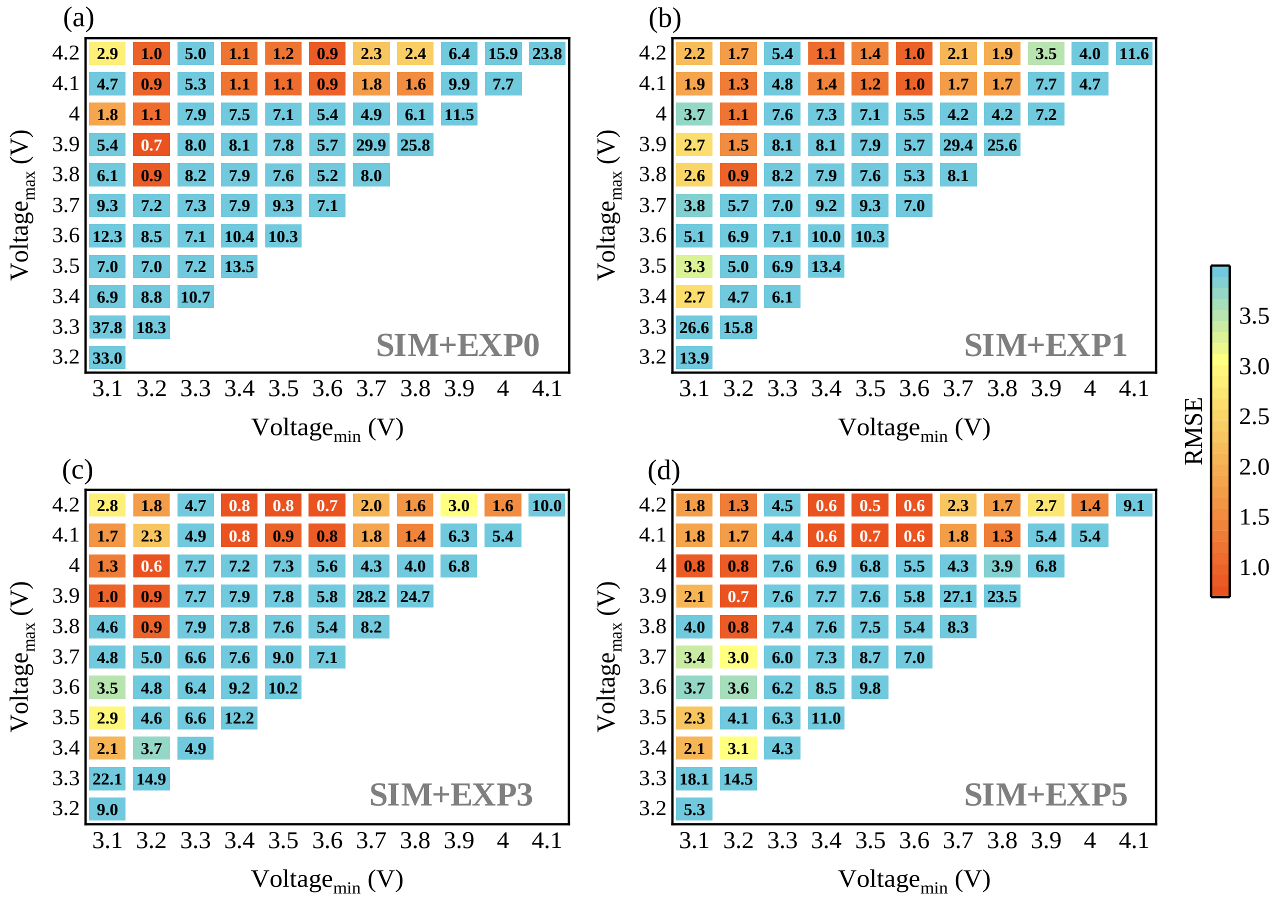

Fig. 6. RMSE values in battery SOH estimation under different voltage windows with the inclusion of early-stage data for condition II: (a) without experimental data; (b)–(d) with experimental data from the first 1, 3, and 5 tests.

corresponds to a 20%-40% SOC window. This indicates that a voltage window of 3.8 V-4.1 V neglects the IC information corresponding to Valley III within this range, where a critical phase transition occurs in the positive electrode material [45, 54].

To summarize, the common voltage window of 3.6 V-4.1 V exhibits significant potential for broad application in battery aging diagnosis. Compared to prior studies of VQ reconstruction within a 20%-70% SOC using partial charge curves, this window roughly corresponds to between 25% and 85% of the SOC. This approach designates a larger termination SOC does not require a smaller starting SOC. This improvement is practically meaningful since batteries are seldom fully discharged before the charging process begins, enabling a slightly larger starting voltage or SOC to be more available. Furthermore, the applicable partial voltage window may depend on the specific battery type. For example, lithium iron phosphate (LFP) batteries generally work under 3.6 V, and thus, the partial window should be lower. Therefore, finding a specific applicable partial voltage window for batteries made of different materials will further enable the diagnosis of battery degradation under normal usage.

5.4 Battery aging diagnosis under high C-rates

In this section, the effectiveness of the framework is assessed using data collected at rates higher than C/30. IC sequences from the extended charging rate tests are utilized for both SOH estimation and degradation mode identification, and the accuracy of the results is discussed. Cells operating at extremely low charging rates are infrequently encountered in real-world scenarios; thus, charging tests at higher rates more closely approach practical applications than previous methods. However, this approach introduces new challenges in the extraction of IC sequences. First, higher charging rates imply large currents, which cause the features of the IC sequence to "drift" towards higher voltages due to the impact of Ohm's law on the internal resistance. The challenge in applying the original IC sequence contributes to inaccuracies in both SOH and degradation modes. Furthermore, higher charging rates exacerbate the inhomogeneity of the electrode during lithiation/delithiation, introducing more complex dynamic impacts. Schmit et al. demonstrated the disappearance of Peak I in the DV curve of NMC-811 with increasing charging rate [16]. To address these challenges, constant voltage offset subtraction is considered an approach for compensating for the VQ curve and correcting IC sequence distortions.

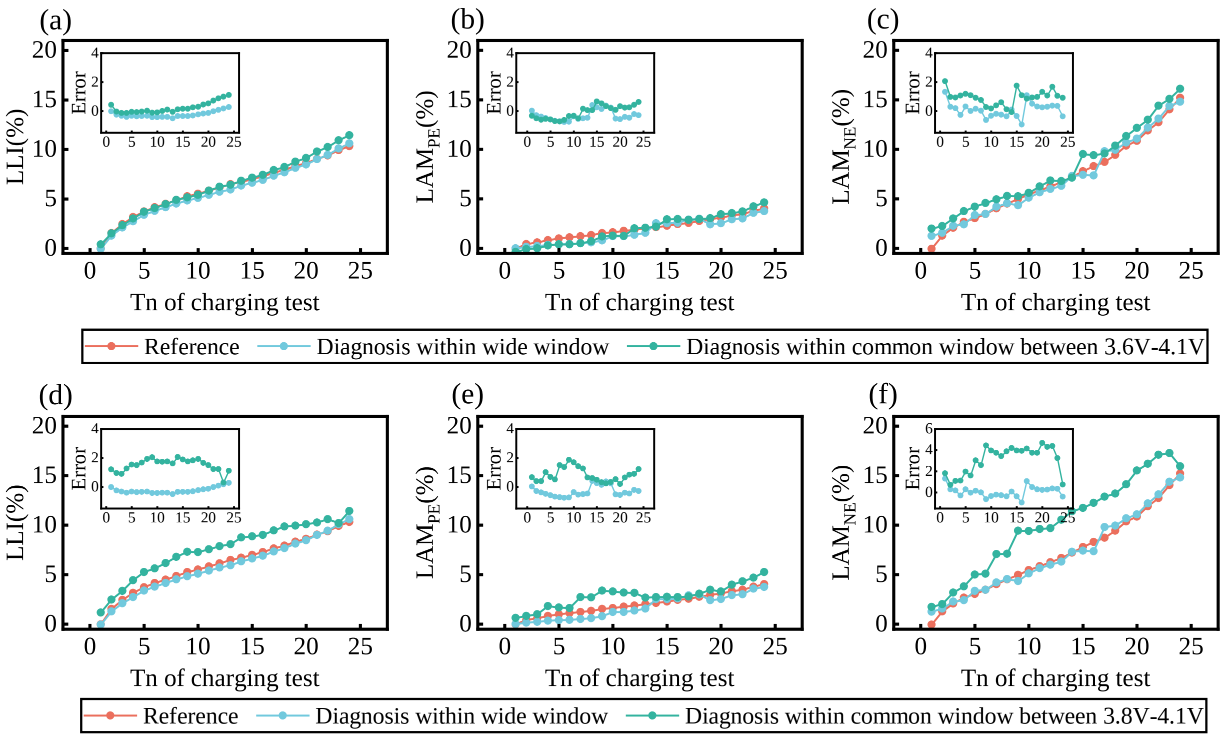

Fig. 7. Degradation modes diagnostic with the proposed framework for cell#75 (Condition II-1) using two selected common voltage windows: (a)-(c) LLI, LAM_{PE} and LAM_{NE} for 3.6-4.1 V; (d)-(e) LLI, LAM_{PE} and LAM_{NE} for 3.8-4.1 V. Tn denotes the n^{th} one of the C/30 rate charging tests.

The diagnoses for Condition II-2 under higher rate tests with and without overpotential compensation in two windows are presented in Fig. 8. The proposed framework achieves these diagnoses by subtracting the constant voltage offset from the charging curve. This adjustment can be similar to realigning the IC sequences and enhancing the suitability for machine learning. Resistance is determined through pulse tests in the aging test sequence, which originates from the 50% SOC. While opting for SOC-dependent resistance could theoretically improve polarization compensation for the charging curve, it inevitably amplifies the model's complexity and introduces more intricate mechanisms [48]. Therefore, overpotential subtraction based on SOC-independent resistance ensures the stability and reliability of the IC sequences.

Figs. 8 (a), 8(c), 8(e) and 8(g) illustrate the different rates of identification within a wide voltage window. The dashed lines represent diagnostics without overpotential compensation, and the solid lines represent

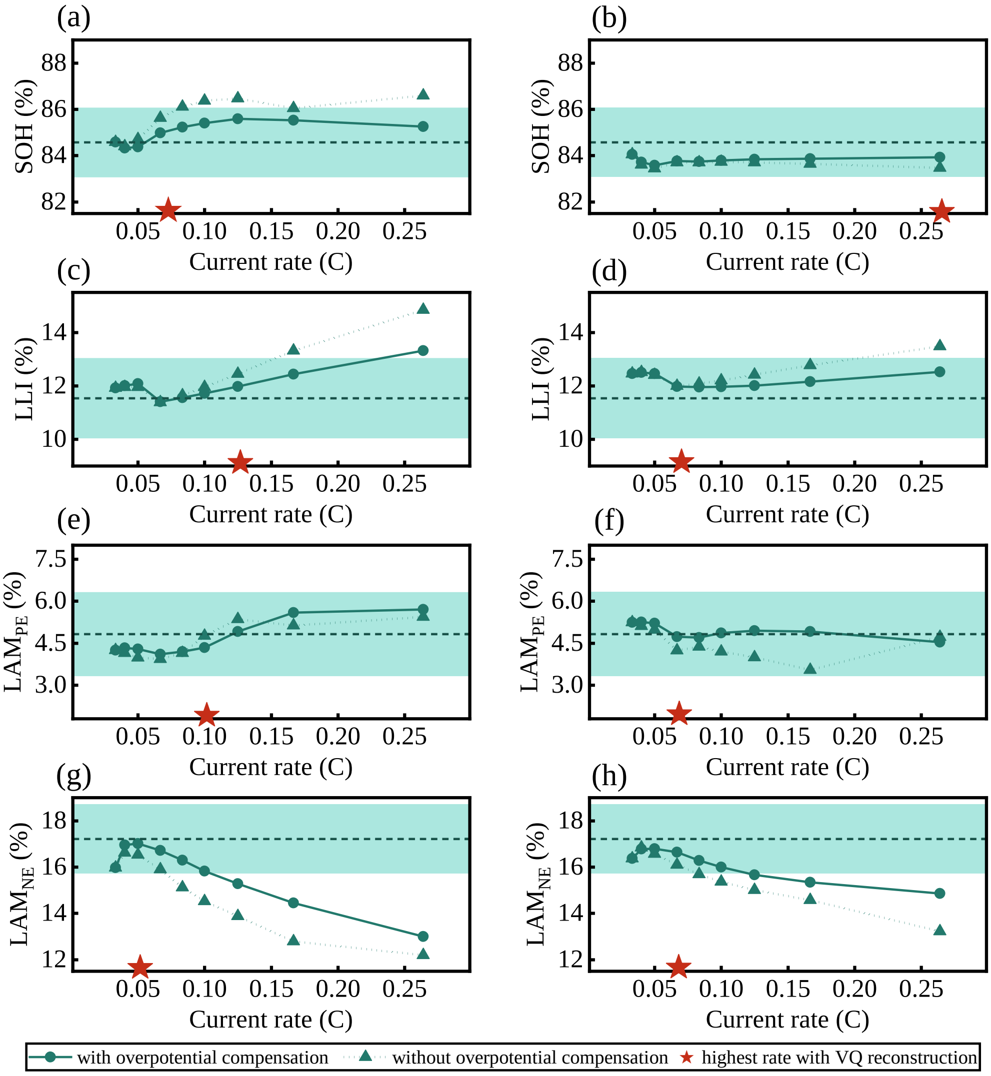

Fig. 8. Degradation diagnosis with the proposed framework with and without overpotential compensation under different rates for cell#76 (Condition II-2): (a)(b) SOH estimation based on wide voltage window 3.5 V-4.2 V and common one 3.6 V-4.1 V; (c)(d) LLI diagnosis based on wide voltage window 3.5 V-4.2 V and common one 3.6 V-4.1 V ; (e)(f) LAM_{PE}; (g)(h) LAM_{NE}

diagnostics with overpotential compensation. The horizontal lines represent true or reference values for the results, assuming that the aging state remains unchanged during continuous extended-rate testing. Shaded regions represent a 1.5% error and are set as an acceptable range for diagnostic accuracy. With increasing rates, disparities between obtainment from the framework and the reference values become more evident. The absence of voltage offset correction renders the IC sequence less informative for higher rates, especially for SOH, LLI and LAM_{NE}. Overpotential compensation significantly reduces this issue to facilitate effective diagnostics for higher-rate tests. For SOH, the original framework estimates fail at C/12, whereas IC correction based on overpotential extends the usable rate to 0.264C, which is similar to that of LLI. The impact of overpotential does not seem to affect LAM_{PE}, possibly because positive electrode aging is not significant and can be identified at higher rates. In contrast, the rapid degradation of the negative electrode material and the dissipation of the charging curve's phase-change peak at high rates hinder LAM_{NE} diagnostics. With overpotential subtraction, the available diagnostic rate for LAM_{NE} can be increased from C/15 to C/10. Table 2 summarizes the diagnostic errors for two cells in the wide voltage window. For specific cells, the rate can even be increased to C/6.

Table 2 SOH estimation error and degradation modes diagnosis error values within the wide voltage window with overpotential compensation under different rates for Condition II.

Charging rate/C	SOH %		LLI %		LAM_{PE} %		LAM_{NE} %	
	II-1	II-2	II-1	II-2	II-1	II-2	II-1	II-2
1/30	0.9	0.7	0.5	0.4	0.1	0.3	0.7	1.2
1/25	1.2	1.0	0.7	0.5	0.2	0.2	0.9	0.3
1/20	1.5	1.0	0.9	0.5	0.1	0.2	1.5	0.2
1/15	1.5	0.8	1.0	0.1	0.2	0.8	1.6	0.5
1/12	1.3	0.7	1.2	0.0	0.0	0.9	1.3	0.9
1/10	1.2	0.4	1.3	0.2	0.0	0.9	0.9	1.4
1/8	1.0	0.2	1.6	0.4	0.1	0.8	0.4	1.9
1/6	1.1	0.3	2.0	0.9	0.8	0.1	0.4	2.8
0.264	1.2	0.0	2.7	1.8	1.5	0.5	2.0	4.2

Figs. 8(b), 8(d), 8(f) and 8(h) show the performance characteristics at different rates within the common charging voltage window of 3.6 V-4.1 V, as specified in Section 5.3. For degradation modes, the overpotential influence persists, but a narrower window allows for higher magnifications, such as those of LLI. With and without overpotential compensation, this phenomenon may be explained by the charging curve reaching the upper cutoff voltage more rapidly at higher rates, compressing the VQ curve. Additionally, differences in resistance within a high SOC window can cause anomalous voltage correction. Excluding the voltage region at the end of charging in the common voltage window mitigates the negative impact of the above description on diagnosis, facilitating the acquisition of degradation modes for higher rates. Table 3 summarizes the diagnostic errors in the common voltage window, with the Condition II-1 SOH estimates exhibiting errors beyond the acceptable range. Condition II-1 performed uniquely during the last test (T24) before the end of the battery life. IC sequences from C/30 provide low-precision SOH, restricting the performance at higher magnifications. Despite these errors exceeding the acceptable range, they remain within 2.5% and exhibit minimal fluctuations as the rates increase. This confirms that the impact of heavy currents on IC sequences is effectively mitigated through overpotential compensation.

Table 3 SOH estimation error and degradation modes diagnosis error values within the common voltage window with overpotential compensation under different rates for Condition II.

Charging rate/C	SOH %		LLI %		LAM_{PE} %		LAM_{NE} %	
	II-1	II-2	II-1	II-2	II-1	II-2	II-1	II-2
1/30	1.4	0.6	1.2	0.9	0.8	0.4	0.3	0.8
1/25	1.9	0.7	1.4	1.0	0.8	0.4	1.0	0.4
1/20	2.3	0.7	1.5	0.9	0.8	0.4	1.5	0.4
1/15	2.5	0.8	1.5	0.4	0.8	0.1	1.5	0.6
1/12	2.5	0.8	1.5	0.4	0.8	0.1	1.2	0.9
1/10	2.5	0.8	1.4	0.4	0.8	0.0	1.0	1.2
1/8	2.5	1.1	1.5	0.5	1.0	0.1	0.6	1.5
1/6	2.4	0.9	1.6	0.6	1.1	0.1	0.3	1.9
0.264	2.2	0.5	1.9	1.0	0.8	0.3	0.2	2.3

In conclusion, diagnosing cell aging for higher rates from charging can be achieved by overpotential compensation, which overcomes the limitations posed by high currents and yields accurate results. The VQ reconstruction method [16] also exhibits widespread applications, establishing an acceptable range with an error threshold of 2% (marked as ⋆ in Fig. 8). Comparatively, while accurate diagnosis is achieved at extremely low rates, incorporating a mechanism model and machine learning expands the potential for higher rates and broader applications within the defined acceptable range.

6. Conclusions

The state of health (SOH) and degradation modes of lithium-ion batteries provide crucial information for their diagnosis and prognosis. The current research is limited by the reliance on a large amount of historical data and the time- and cost-consuming tests of low-current charging/discharging for calibration data collection. We propose an integrated framework for degradation diagnosis that combines a mechanistic model with machine learning. Using synthetic data generated from the mechanistic model, data-driven SOH estimation and automatic degradation mode identification are achieved using this approach.

In this study, a synthetic dataset for a nickel-rich NMC-811 battery was generated based on a mechanistic model by presetting different degradation modes, including approximately 4800 sets covering many possible aging paths. Employing a Gaussian process framework, we extracted incremental capacity sequences as inputs for indicating the battery SOH and degradation modes. Data augmentation using a limited amount of early experimental data enhanced the SOH estimation precision, bridging the gap between digital twin models and real-world cells. Moreover, due to the differences between the sensitivities of the modes to voltage responses, the multistep diagnosis method uses a series of machine learning models to identify the modes sequentially based on qualitative analysis, decoupling the complex interactions between multiple degradation modes. Overpotential correction is incorporated to further improve the degradation diagnosis performance of the method under normal usage conditions, i.e., common voltage windows with large current rates.

The framework was validated with 6 cells under different operating conditions. After incorporating a limited amount of early experimental data, the results demonstrated an accurate SOH estimation with an RMSE values of less than 2% in the common voltage window of 3.6 V-4.1 V, roughly corresponding to the 25%-85% state of charge (SOC) window. This framework can also be adapted to degradation modes, and the multistep diagnosis method yields convenient and automatic diagnoses with higher estimation accuracy than does the differential voltage fitting method. The proposed framework can estimate accurate battery degradation modes with an error of 1.5% under a high current rate of up to C/4 in some scenarios.

In future work, the diagnostic framework will be validated and applied to more batteries and aging conditions. We will conduct experiments under various conditions for more comprehensive degradation diagnosis and rate analysis. This approach is expected to overcome the current validation limitation due to the limited number of cells and to further improve the method performance. Overall, this research highlights the reliable SOH estimation and degradation mode identification achieved by using synthetic data and a developed multistep diagnostic method. This synthesis provides comprehensive insight into battery degradation, demonstrating the significant potential of combining machine learning with mechanistic models for rapid and accurate aging diagnosis.

CRediT authorship contribution statement

Ze Wu: Methodology, Software, Validation, Visualization, Writing-original draft.
Yongzhi Zhang: Conceptualization, Supervision, Methodology, Writing-reviewing&editing.
Huizhi Wang: Writing-reviewing&editing, Supervision, Investigation.

Declaration of competing interest

The authors declare that they have no known competing financial interests or personal relationships that could have appeared to influence the work reported in this paper.

Data availability

The datasets used in this study are available at https://mediatum.ub.tum.de/1690455. The core codes of this study can be found at https://data.mendeley.com/datasets/mjy453j33n/1.

Acknowledgement

This work was supported by the National Natural Science Foundation of China (No. 52307234). The dataset used in this study is sourced from Julius Schmitt and colleagues from the Technical University of Munich.

Appendix A

Degradation modes involve various aging mechanisms within lithium-ion batteries and provide valuable information for path-dependent degradation [9]. The modes are generally defined as LLI and LAM of positive and negative electrodes (LAM_{PE}, LAM_{NE}) [13]. The degradation modes include thermodynamic aging of the battery and do not consider the kinetic behavior, because kinetic degradation involves an increase in impedance, which can be measured by the voltage response [9]. Fig. 1 illustrates the different degradation mechanisms and their associated degradation modes. The details are as follows:

Loss of lithium inventory (LLI): Active lithium ions are consumed in the side reaction and are not able to cycle between the positive and negative electrodes. The growth of the SEI layer and irreversible lithium plating are the primary factors in this process. The SEI layer emerges from the reduction reaction of Li^+ at the negative electrode-electrolyte interface, and irreversible lithium plating is associated with higher rates and lower temperatures. If lithium ions are trapped in electrically insulating particles of the active material, an LLI is also present. Since lithium ions are no longer available, the LLI is directly related to capacity loss.

Loss of active materials (LAM): The failure of the active material occurs in both the positive electrode and negative electrode, i.e., LAM_{PE} and LAM_{NE}, respectively. Particle cracking, structural disorder, and loss of electrical contact render the electrode's active material incapable for the insertion and extraction of lithium ions. Failures in other components, such as binders and current collectors, can also lead to LAM. LAM further causes capacity loss.

Appendix B

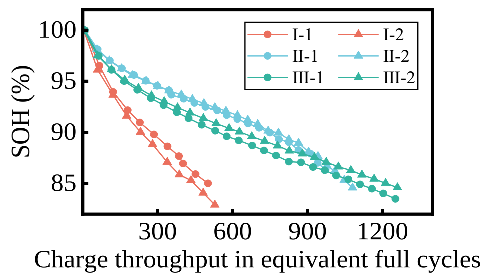

Fig. B.1. SOH of the 6 cells determined based on the charging capacity at C/30 from the aging test sequence.

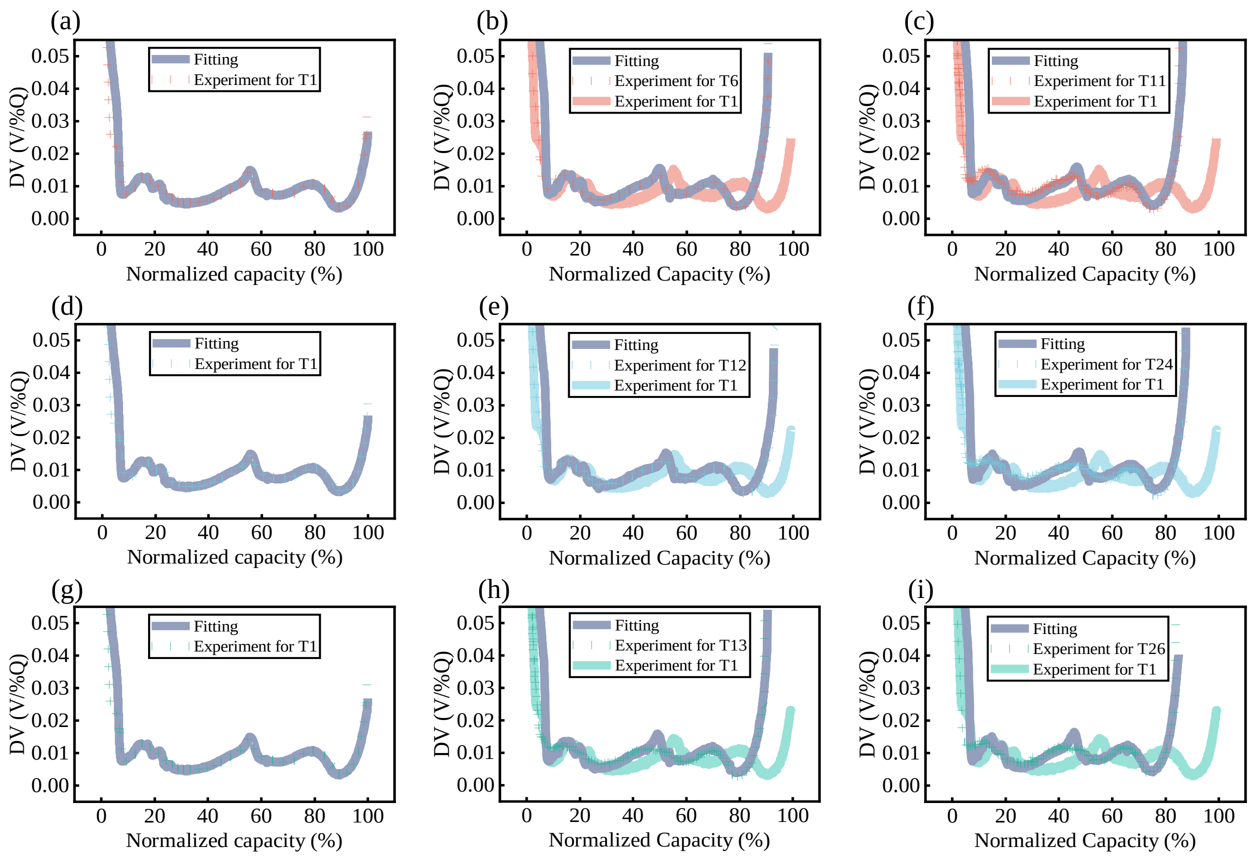

Fig. B.2. The processes of experimental and simulated fitting for 3 cells from different conditions. (a)-(c) Fitting for T1, T6 and T11 from Condition I-1; (d) –(f) Fitting for T1, T12 and T24 from Condition II-1; (g)-(i) Fitting for T1, T13 and T26 from Condition III-1.

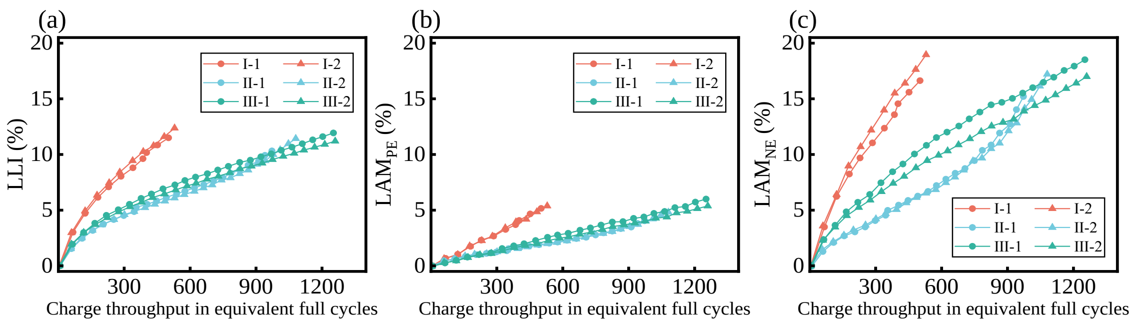

Fig. B.3. The reference values of degradation modes obtained from the model fitting, and the relationships between them and the total charge throughput for 6 cells. (a) LLI; (b)LAM_{PE}; (c)LAM_{NE}.

Appendix C

The mechanistic modeling in the manuscript used the OCP of the pristine composite negative electrode for simplification. It is acknowledged that the pristine OCP is from the fresh half-cell and thus does not distinguish the degradation differences between graphite and silicon in the negative electrode, i.e., $LAM_{NE\text{-}Gr}$ for graphite and $LAM_{NE\text{-}Si}$ for silicon. Therefore, the impact of simplified modeling in the proposed diagnosis framework needs to be explained and discussed. This appendix builds a mechanistic model based on a Si/C blended negative electrode and compares $LAM_{NE\text{-}Gr}$ considering silicon to LAM_{NE} without differentiating the composite electrode materials. The aim of this appendix is to explain the feasibility and effectiveness of the developed method by achieving battery degradation diagnostics under typical operating conditions while acknowledging its limitations.

C.1 Si/C blended-based mechanistic model and degradation analysis

Schmitt et al. used a silicon component to construct a blended negative electrode in tested cells [48]. For blended electrodes, the capacity of the blended negative electrode $Q_{n-blend}$ was constructed by adding silicon and graphite as capacity fractions during lithiation:

$$Q_{n-blend}(U) = \alpha_{Si} \cdot Q_{Si}(U) + (1 - \alpha_{Si})Q_{Gr}(U), \tag{C.1}$$

where α_{Si} is the fraction of silicon in the negative electrode OCP curve, and its shape is influenced by the silicon content, with a lower value resulting in curves of blended electrodes resembling those of pure graphite electrodes. $LAM_{NE\text{-}Gr}$ and $LAM_{NE\text{-}Si}$ are thus defined as the reduction in the percentage of graphite $Q_{Gr}(U)$ and silicon $Q_{Si}(U)$, respectively.

The full-cell VQ curves of the experimental cells were constructed based on the model using the blended negative electrode and NMC-811 positive electrode. Comparing $Q_{n-blend}(U)$ with different silicon fractions α_{Si} to the half-cell of the pristine negative electrode, the silicon capacity fraction α_{Si} is approximately 9%. Fig. C.1 shows the measured and simulated IC and DV curves calculated from the VQ curves. Dubarry et al. previously constructed a mechanistic model for NMC-811 and silicon-graphite batteries [52]. The characteristics of the degradation modes on the IC curve were summarized and included LLI, LAM_{PE}, $LAM_{NE\text{-}Gr}$ and $LAM_{NE\text{-}Si}$. Similarly, Zilberman et al. analyzed the calendar aging of such batteries using DV curves [47]. These studies collectively revealed that the electrochemically active features of silicon were particularly significant in low-voltage and low-SOC windows. These characteristics can be used to quantify the $LAM_{NE\text{-}Si}$ and $LAM_{NE\text{-}Gr}$ by matching the simulated IC/DV from the mechanistic model with the experimental data.

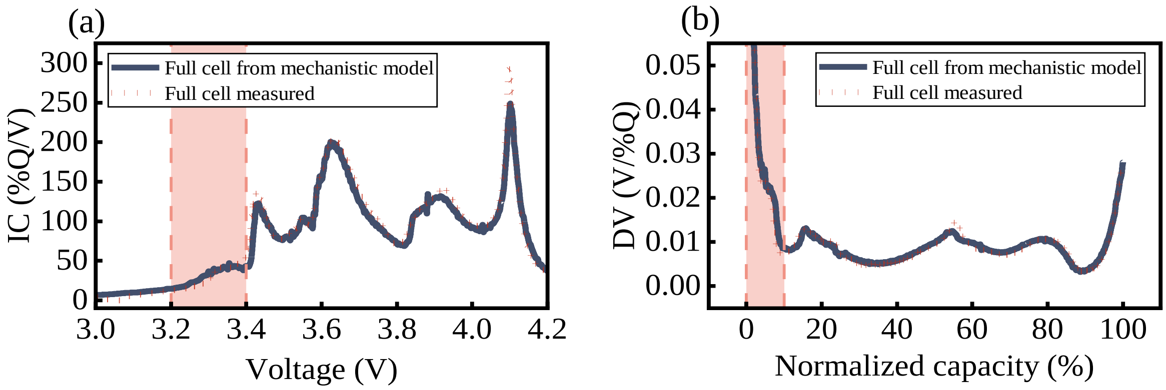

Fig. C.1. Comparison of the charging of battery C/30 and the mechanistic model simulation based on blended negative electrode. (a) IC; (b) DV.

C.2 Comparison of the different degradation modes

The Si/C blended-based mechanistic model is applied for the reference values of the degradation modes. LLI, LAM_{PE}, $LAM_{NE\text{-}Si}$ and $LAM_{NE\text{-}Gr}$ were adjusted to manually fit the experimental and synthesized DV curves.

The low-voltage and low-SOC windows for silicon activity were additionally used to identify LAM_{NE-Si} and LAM_{NE-Gr}, respectively. Fig. C.2 shows the reference values obtained using the blended negative electrode. Compared with Fig. B.3, LLI and LAM_{PE} were not significantly affected when the pristine negative electrode or the blended electrode was used. Fig. C.2 (d) shows an increase in LAM_{NE-Si} during cycling; this result indicates a faster degradation of silicon particles compared to that of graphite. The imbalance of degradation may be related to the more severe volumetric change in silicon and the greater current density [49-51].

Furthermore, the voltage window of battery cycling also affects LAM_{NE-Si}. The silicon loss of the two cells under Condition II cycling within 3.6 V-4.2 V is slower. This is expected because this cycling voltage window does not include the active potential window of Si, which is 3.2-3.4 V; thus, more charging throughput is involved in the lithiation and delithiation of graphite than silicon. Conditions I (2.5 V-4.2 V) and III (2.5 V-4.0 V) both include the active windows of Si; however, due to more equivalent cycles obtained in Condition III than in Condition I, the loss of silicon particles under Condition III is slightly greater. A comparison of the LAM_{NE} in Fig. B.3 with the graphite LAM_{NE-Gr} in Fig. C.2(d) shows a difference of 3%. This result aligns with those from previous studies [48], demonstrating a slight overestimation of graphite loss in the current diagnostics of LAM_{NE}.

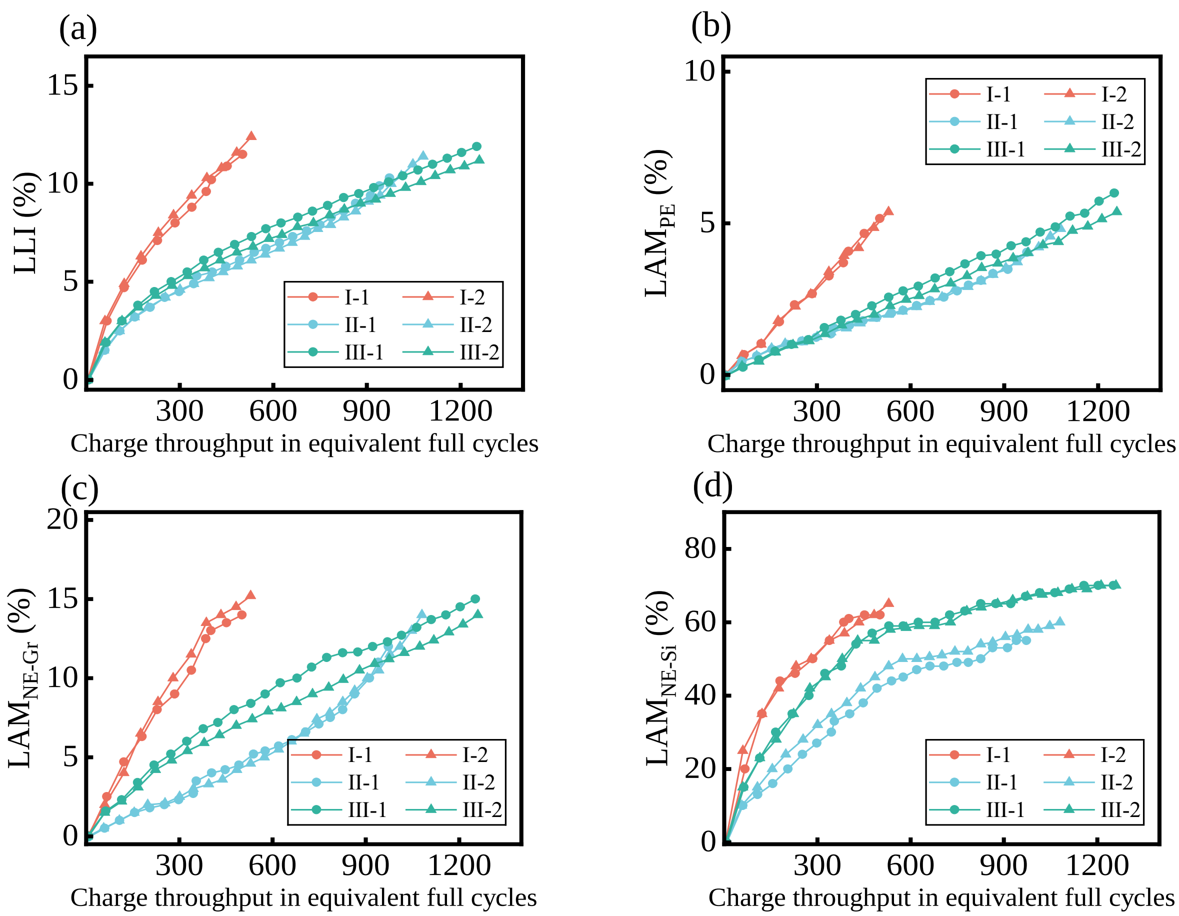

Fig. C.2. Reference values of LLI (a), LAM_{PE} (b), LAM_{NE-Gr} (c) and LAM_{NE-Si} (d) obtained from the blended negative electrode model fitting, and the relationships between each and the total charge throughput for 6 cells.

C.3 Conclusive Comments

This appendix provides the Si/C blended-based mechanistic model and an analysis of the different losses of graphite and silicon, LAM_{NE-Gr} and LAM_{NE-Si}, respectively. The slight difference between LAM_{NE-Gr} and LAM_{NE} indicates that although information on silicon loss is missing, the quantification of LAM_{NE} using pristine

OCP curves of the composite negative electrode is sufficiently accurate to reflect the graphite loss; here, the graphite material constitutes more than 90% of the negative electrode. In summary, the proposed diagnostic framework aims to achieve accurate degradation modes and SOH estimations for aged cells using data commonly observed under actual usage conditions and includes partial charging data with high current rates. In practice, partial charging data generally do not cover the electrochemically active window of silicon, i.e., a low-voltage window within 3.2-3.4 V and a low-SOC window within 0-15%. Therefore, the diagnostic framework assesses the degradation of graphite (with slight overestimation) and does not include the loss of silicon. Moreover, the simplified mechanistic model has been widely applied [16, 47, 53], providing valuable results and reliable insights into battery material degradation.

References

[1] Q. Yu, Y. Huang, A. Tang, C. Wang, W. Shen, IEEE Trans. Intell. Transp. Syst., 24 (2023) 6362-6371, https://doi.org/10.1109/tits.2023.3252164.

[2] Y. Zhang, M. Zhao, Energy Storage Mater., 57 (2023) 346-359, https://doi.org/10.1016/j.ensm.2023.02.035.

[3] C. Zhang, L. Luo, Z. Yang, S. Zhao, Y. He, X. Wang, H. Wang, Green Energy and Intelligent Transportation, 2 (2023), https://doi.org/10.1016/j.geits.2023.100108.

[4] Y. Zhang, X. Feng, M. Zhao, R. Xiong, J. Power Sources, 577 (2023), https://doi.org/10.1016/j.jpowsour.2023.233246.

[5] M. Killer, M. Farrokhseresht, N.G. Paterakis, Appl. Energy, 260 (2020), https://doi.org/10.1016/j.apenergy.2019.114166.

[6] C. Chen, R. Xiong, R. Yang, H. Li, Green Energy and Intelligent Transportation, 1 (2022), https://doi.org/10.1016/j.geits.2022.100001.

[7] S. Ding, Y. Li, H. Dai, L. Wang, X. He, Adv. Energy Mater., 13 (2023), https://doi.org/10.1002/aenm.202301452.

[8] A. Barré, B. Deguilhem, S. Grolleau, M. Gérard, F. Suard, D. Riu, J. Power Sources, 241 (2013) 680-689, https://doi.org/10.1016/j.jpowsour.2013.05.040.

[9] C.R. Birkl, M.R. Roberts, E. McTurk, P.G. Bruce, D.A. Howey, J. Power Sources, 341 (2017) 373-386, https://doi.org/10.1016/j.jpowsour.2016.12.011.

[10] C. Pastor-Fernández, T.F. Yu, W.D. Widanage, J. Marco, Renewable Sustainable Energy Rev., 109 (2019) 138-159, https://doi.org/10.1016/j.rser.2019.03.060.

[11] M. Dubarry, V. Svoboda, R. Hwu, B.Y. Liaw, Electrochem. Solid-State Lett., 9 (2006) A454,

[12] M. Dubarry, B.Y. Liaw, J. Power Sources, 194 (2009) 541-549, https://doi.org/10.1016/j.jpowsour.2009.05.036.

[13] M. Dubarry, C. Truchot, B.Y. Liaw, J. Power Sources, 219 (2012) 204-216, https://doi.org/10.1016/j.jpowsour.2012.07.016.

[14] M. Dubarry, D. Beck, Accounts Mater. Res., 3 (2022) 843-853, https://doi.org/10.1021/accountsmr.2c00082.

[15] C.R. Birkl, E. McTurk, M.R. Roberts, P.G. Bruce, D.A. Howey, J. Electrochem. Soc., 162 (2015) A2271-A2280, https://doi.org/10.1149/2.0331512jes.

[16] J. Schmitt, M. Rehm, A. Karger, A. Jossen, J. Energy Storage, 59 (2023), https://doi.org/10.1016/j.est.2022.106517.

[17] C. Zhu, L. Sun, C. Chen, J. Tian, W. Shen, R. Xiong, Electrochim. Acta, 459 (2023), https://doi.org/10.1016/j.electacta.2023.142588.

[18] S. Yang, C. Zhang, J. Jiang, W. Zhang, Y. Gao, L. Zhang, J. Energy Storage, 35 (2021), https://doi.org/10.1016/j.est.2021.102271.

[19] G. Seo, J. Ha, M. Kim, J. Park, J. Lee, E. Park, S. Bong, K. Lee, S.J. Kwon, S.-p. Moon, J. Choi, J. Lee, J. Energy Chem., 67 (2022) 663-671, https://doi.org/10.1016/j.jechem.2021.11.009.

[20] C. Pastor-Fernández, W.D. Widanage, J. Marco, M.-A. Gama-Valdez, G.H. Chouchelamane, in: 2016 IEEE Transportation Electrification Conference and Expo (ITEC), IEEE, 2016, pp. 1-6.

[21] B. Wu, V. Yufit, Y. Merla, R.F. Martinez-Botas, N.P. Brandon, G.J. Offer, J. Power Sources, 273 (2015) 495-501, https://doi.org/10.1016/j.jpowsour.2014.09.127.

[22] R. Prosser, G. Offer, Y. Patel, J. Electrochem. Soc., 168 (2021), https://doi.org/10.1149/1945-7111/abed28.

[23] M. Dubarry, M. Berecibar, A. Devie, D. Anseán, N. Omar, I. Villarreal, J. Power Sources, 360 (2017) 59-69, https://doi.org/10.1016/j.jpowsour.2017.05.121.

[24] M. Dubarry, D. Beck, J. Power Sources, 479 (2020), https://doi.org/10.1016/j.jpowsour.2020.228806.

[25] M. Dubarry, D. Beck, Energies, 14 (2021), https://doi.org/10.3390/en14092371.

[26] X. Lu, J. Qiu, G. Lei, J. Zhu, IEEE Transactions on Transportation Electrification, 9 (2023) 1142-1152, https://doi.org/10.1109/tte.2022.3196087.

[27] K.S. Mayilvahanan, K.J. Takeuchi, E.S. Takeuchi, A.C. Marschilok, A.C. West, Batteries & Supercaps, 5 (2021),

https://doi.org/10.1002/batt.202100166.
[28] C. Wang, Y. Chen, W. Luan, S. Li, Y. Yao, H. Chen, eTransportation, 18 (2023), https://doi.org/10.1016/j.etran.2023.100281.
[29] N. Costa, D. Anseán, M. Dubarry, L. Sánchez, J. Power Sources, 592 (2024), https://doi.org/10.1016/j.jpowsour.2023.233910.
[30] N. Costa, L. Sánchez, D. Anseán, M. Dubarry, J. Energy Storage, 55 (2022), https://doi.org/10.1016/j.est.2022.105558.
[31] M. Dubarry, N. Costa, D. Matthews, Nat Commun, 14 (2023) 3138, https://doi.org/10.1038/s41467-023-38895-7.
[32] A. Thelen, Y.H. Lui, S. Shen, S. Laflamme, S. Hu, H. Ye, C. Hu, Energy Storage Mater., 50 (2022) 668-695, https://doi.org/10.1016/j.ensm.2022.05.047.
[33] H. Ruan, J. Chen, W. Ai, B. Wu, Energy and AI, 9 (2022), https://doi.org/10.1016/j.egyai.2022.100158.
[34] R. Xu, Y. Wang, Z. Chen, Batteries, 9 (2023), https://doi.org/10.3390/batteries9020129.
[35] S. Kim, Z. Yi, B.-R. Chen, T.R. Tanim, E.J. Dufek, Energy Storage Mater., 45 (2022) 1002-1011, https://doi.org/10.1016/j.ensm.2021.07.016.
[36] W. Li, J. Chen, K. Quade, D. Luder, J. Gong, D.U. Sauer, Energy Storage Mater., 53 (2022) 391-403, https://doi.org/10.1016/j.ensm.2022.08.021.
[37] J. Sturm, A. Rheinfeld, I. Zilberman, F.B. Spingler, S. Kosch, F. Frie, A. Jossen, J. Power Sources, 412 (2019) 204-223, https://doi.org/10.1016/j.jpowsour.2018.11.043.
[38] I. Bloom, A.N. Jansen, D.P. Abraham, J. Knuth, S.A. Jones, V.S. Battaglia, G.L. Henriksen, J. Power Sources, 139 (2005) 295-303, https://doi.org/10.1016/j.jpowsour.2004.07.021.
[39] I. Bloom, L.K. Walker, J.K. Basco, D.P. Abraham, J.P. Christophersen, C.D. Ho, J. Power Sources, 195 (2010) 877-882, https://doi.org/10.1016/j.jpowsour.2009.08.019.
[40] H.M. Dahn, A.J. Smith, J.C. Burns, D.A. Stevens, J.R. Dahn, J. Electrochem. Soc., 159 (2012) A1405-A1409, https://doi.org/10.1149/2.013209jes.
[41] K. Honkura, H. Honbo, Y. Koishikawa, T. Horiba, ECS Transactions, 13 (2008) 61, https://doi.org/10.1149/1.3018750.
[42] M. Dubarry, D. Beck, Front. Energy Res., 10:1023555 (2022), https://doi.org/10.3389/fenrg.2022.1023555.
[43] A. Devie, G. Baure, M. Dubarry, Energies, 11 (2018), https://doi.org/10.3390/en11051031.
[44] R. Jung, M. Metzger, F. Maglia, C. Stinner, H.A. Gasteiger, J. Electrochem. Soc., 164 (2017) A1361-A1377, https://doi.org/10.1149/2.0021707jes.
[45] M. Schindler, J. Sturm, S. Ludwig, A. Durdel, A. Jossen, J. Electrochem. Soc., 168 (2021), https://doi.org/10.1149/1945-7111/ac03f6.
[46] J. Schmitt, M. Schindler, A. Jossen, J. Power Sources, 506 (2021), https://doi.org/10.1016/j.jpowsour.2021.230240.
[47] I. Zilberman, J. Sturm, A. Jossen, J. Power Sources, 425 (2019) 217-226, https://doi.org/10.1016/j.jpowsour.2019.03.109.
[48] J. Schmitt, M. Schindler, A. Oberbauer, A. Jossen, J. Power Sources, 532 (2022), https://doi.org/10.1016/j.jpowsour.2022.231296.
[49] N. Kirkaldy, M.A. Samieian, G.J. Offer, M. Marinescu, Y. Patel, ACS Applied Energy Materials, 5 (2022) 13367-13376, https://doi.org/10.1021/acsaem.2c02047.
[50] A.Y.R. Prado, M.-T.F. Rodrigues, S.E. Trask, L. Shaw, D.P. Abraham, J. Electrochem. Soc., 167 (2020), https://doi.org/10.1149/1945-7111/abd465.
[51] V.A. Sethuraman, A. Nguyen, M.J. Chon, S.P.V. Nadimpalli, H. Wang, D.P. Abraham, A.F. Bower, V.B. Shenoy, P.R. Guduru, J. Electrochem. Soc., 160 (2013) A739-A746, https://doi.org/10.1149/2.021306jes.
[52] D. Anseán, G. Baure, M. González, I. Cameán, A.B. García, M. Dubarry, J. Power Sources, 459 (2020), https://doi.org/10.1016/j.jpowsour.2020.227882.
[53] F. Wang, S. Tang, X. Han, L. Lu, C. Yu, C. Zhao, Y. Gao, G. Zhu, K. Zhuang, M. Ouyang, J. Power Sources, 588

(2023), https://doi.org/10.1016/j.jpowsour.2023.233744.
[54] M. Schindler, J. Sturm, S. Ludwig, J. Schmitt, A. Jossen, eTransportation, 8 (2021), https://doi.org/10.1016/j.etran.2020.100102.